Ordered sphalerite derivative $Cu_5Sn_2S_7$: a degenerate semiconductor with high carrier mobility in the Cu-Sn-S diagram

Ventrapati Pavan Kumar,[a] Pierric Lemoine,[b] Virginia Carnevali,[c] Gabin Guélou,[a] Oleg I. Lebedev,[a] Philippe Boullay,[a] Bernard Raveau,[a] Rabih Al Rahal Al Orabi,[c,d] Marco Fornari,[c] Carmelo Prestipino,[b] Denis Menut,[e] Christophe Candolfi,[f] Bernard Malaman,[f] Jean Juraszek,[g] Emmanuel Guilmeau*[a]*

[a] CRISMAT, CNRS, Normandie Univ, ENSICAEN, UNICAEN, 14000 Caen, France

Email: Emmanuel.guilmeau@ensicaen.fr

[b] Univ Rennes, CNRS, ISCR – UMR 6226, F-35000 Rennes, France

[c] Department of Physics and Science of Advanced Materials Program, Central Michigan University, Mt. Pleasant, MI 48859, USA

Email: forna1m@cmich.edu

[d] Solvay, Design and Development of Functional Materials Department, Axel'One, 87 avenue des Frères Perret, 69192 Saint Fons, Cedex, France

[e] Synchrotron SOLEIL, Ligne MARS, L'Orme des Merisiers, Saint Aubin, 91192 Gif-sur-Yvette, France

[f] Institut Jean Lamour, UMR 7198 CNRS – Université de Lorraine, 2 allée André Guinier-Campus ARTEM, BP 50840, 54011 Nancy Cedex, France

[g] GPM, CNRS, Univ Rouen, INSA Rouen, UNIROUEN, 76000 Rouen, France

Electronic supplementary information (ESI) available. See DOI:10.1039/d1ta01615f

Abstract

Regardless the complexity of the phase diagram of the Cu-Sn-S system, several compositions near the prototypical mohite Cu_2SnS_3 have arisen as potential non-toxic, earth-abundant and cost-efficient photovoltaic and thermoelectric materials. In this work, we revisited the $Cu_{2+x}Sn_{1-x}S_3$ system and discovered a monoclinic ($C2$) ordered sphalerite derivative member, $Cu_5Sn_2S_7$. Using a combination of synchrotron diffraction and spectroscopy, transmission electron microscopy, precession-assisted electron diffraction tomography, Mössbauer spectroscopy, first principles calculations and transport properties measurements, we discuss the structure-thermoelectric properties relationships and clarify the interesting crystal chemistry in this system. The ternary sulfide $Cu_5Sn_2S_7$ exhibits a degenerate semiconducting behavior with exceptionally high hole mobility originating from the interplay between atomic ordering and charge delocalization.

1. Introduction

Copper tin sulfides (CTS) represent a very attractive class of materials that have been intensively studied for their promising photovoltaic and thermoelectric properties due to the fact that they exhibit decent performances and consist of non-toxic, ecofriendly and earth-abundant elements.[1–3] Early studies of the Cu-Sn-S system have discussed the existence of numerous phases: Cu_2SnS_3, $Cu_2Sn_2S_5$, Cu_5SnS_4, $Cu_2Sn_3S_7$, Cu_4SnS_4, $Cu_5Sn_2S_7$, $Cu_7Sn_3S_{10}$, Cu_4SnS_6, Cu_3SnS_4, $Cu_{9.67}Sn_{2.33}S_{13}$, $Cu_{10}Sn_2S_{13}$, $CuSn_{3.75}S_8$, $Cu_2Sn_4S_9$, Cu_8SnS_6, $Cu_2Sn_{3.34}S_{7.6}$, $Cu_{10}Sn_2S_{13}$, Cu_5SnS_6, $Cu_4Sn_3S_8$, $Cu_2Sn_2S_9$, $Cu_8Sn_3S_{12}$, $Cu_4Sn_7S_{16}$.[4–16] However, this rich phenomenology has not been greatly exploited in applications mostly because of the limited understanding of the structure-property relationships. The ability to control structural and electronic properties by tuning the Cu/Sn compositional ratio is of paramount importance for achieving efficient thermoelectric (TE) conversion as well as for tuning CTS compositions for thin-film solar cells. Indeed, many copper-tin sulfides have interesting *p*-type transport properties, making them potential candidates for integration in TE modules. In this respect, the sulfide Cu_2SnS_3 exhibits competitive TE performances when doped with Zn and Co, leading to figure of merit *ZT* values of 0.58 and 0.85 at 723 K, respectively.[1,17] Note that the conversion efficiency of TE materials is represented by the figure of merit $ZT = S^2T/\rho\kappa$ (T being the temperature, S the Seebeck coefficient, ρ the electrical resistivity, and κ the thermal conductivity). From the point of view of photovoltaic (PV) applications, CTS materials provide high absorption coefficient, unique tunability of the electronic band gap from 0.9 to 1.77 eV and were predicted to reach a Shockley–Queisser limit of 30% [See Ref.[2] and references therein]. The intrinsic tunability of the functional properties of CTS compounds is due to the complex crystal chemistry, which in most cases, involves a subtle balance

of electrostatic interactions and charge delocalization controlled by the position of Sn^{4+} on the cationic sublattice of corner-sharing tetrahedral network (in most of those compounds).

The remarkable polymorphism of Cu_2SnS_3, which involves three types of symmetry (a high temperature cubic form isotypic with the ZnS structure,[5,7,8] a room temperature tetragonal $I\bar{4}2m$ form,[6] and a monoclinic Cc form[18]), is thought to be due to order-disorder phenomena that significantly influence the electronic transport properties.[1,19] However, in a recent study of the thermoelectric properties of $Cu_{2+x}Sn_{1-x}S_3$, Deng *et al*. have shown that, for $0.016 \leq x \leq 0.08$, the proportion of the three coexisting polymorphs, cubic $F\bar{4}3m$, tetragonal $I\bar{4}2m$, and monoclinic Cc, has surprisingly little influence on the electrical transport properties of the material.[20] Considering the critical effect on the transport properties caused by the modifications of the conductive network observed in colusites,[21–23] we have revisited the $Cu_{2+x}Sn_{1-x}S_3$ system. Using a synergy between synthesis, characterization, and first principles calculations, we found that the crystal chemistry critically controls long range ordering phenomena limiting the relative stability of disordered solid solutions. We discovered an ordered phase $Cu_5Sn_2S_7$ crystallizing with a monoclinic structure described in the space group $C2$. This phase is isotypic to both $Cu_4NiSi_2S_7$,[24] and to the homologous selenide $Cu_5Sn_2Se_7$,[25] and can be obtained as a pure phase for $x = 0.15$. Despite the close compositions and common structural sphalerite framework, the new member of the Cu-Sn-S family is immiscible. We also demonstrate that the electronic transport properties of synthetic mohite Cu_2SnS_3 ($x = 0$, monoclinic Cc), $Cu_{2.075}Sn_{0.925}S_3$ ($x = 0.075$), and $Cu_5Sn_2S_7$ ($x = 0.15$ in $Cu_{2+x}Sn_{1-x}S_3$, monoclinic $C2$) are different and depend on the interplay between the structure and hole carrier concentration,[26] which influences the hybridized 3*d*(Cu)-3*p*(S) conductive network.[27] The discovery of the monoclinic $Cu_5Sn_2S_7$ phase adds a high mobility member to the Cu-Sn-S diagram

and demonstrates how crystal structure can be advantageously manipulated to design novel compositions for energy-oriented applications.

2. Experimental Section

Materials Synthesis

The polycrystalline sample of pristine Cu_2SnS_3 was synthesized by a two-step solid state reaction in evacuated silica tubes from the elemental precursors (Cu (99%, Alfa Aesar), Sn (99.85%, Alfa Aesar), and S (99.5%, Alfa Aesar)). First, Cu, Sn and S were ground in an agate mortar with the appropriate stoichiometric ratio and compacted into a pellet, sealed in an evacuated silica tube and heated to 1023 K at a rate of 50 K min^{-1}. The pellet was held at that temperature for 48h followed by a cooling step down to room temperature at a rate of 50 K min^{-1}. Subsequently, the as-prepared Cu_2SnS_3 sample was crushed and the powder was compacted for a second firing carried out at 873 K for 24h with an intermediate step at 673 K for 12h. The same heating and cooling rates of 50 K min^{-1} were used. The obtained sample was once again ground and sieved down to 200 μm to remove large agglomerates.

Powders of $Cu_{2+x}Sn_{1-x}S_3$ (x = 0.075 and 0.15) were synthesized by mechanical-alloying. All sample preparations and handling of powders were performed in an argon filled glovebox with oxygen content <1 ppm. Stoichiometric amounts of high purity elements Cu (99%, Alfa Aesar), Sn (99.85%, Alfa Aesar), and S (99.5%, Alfa Aesar) were loaded in a 25 mL tungsten carbide jar containing 7 balls of 10 mm under argon atmosphere. High-energy ball-milling was performed in a Fritsch Pulverisette 7 Premium line planetary ball-mill operating at room temperature (RT) at a disc rotation speed of 600 rpm during 6 h. The resulting powders were then ground and sieved down to 150 μm.

The pristine (x = 0) and Cu-rich (x = 0.075 and 0.15) powders were then placed in a graphite die of 10 mm diameter and densified by SPS (FCT HPD 25) at 873 K for 30 min under a pressure of 64 MPa. The final dimensions of the pellet are around 8 mm in thickness and 10 mm in diameter. Relative densities are about 96% for x = 0 sample and 91-92% for x = 0.075 and 0.15 samples.

X-ray diffraction analysis

X-ray powder diffraction (XRPD) data were collected at room temperature using a Bruker D8 Advance Vario 1 two-circle diffractometer (θ-2θ Bragg-Brentano mode) using Cu Kα radiation (λ = 1.5406 Å) equipped with a Ge(111) monochromator (Johansson type) and a Lynx Eye detector. Synchrotron XRPD data of $Cu_5Sn_2S_7$ ($Cu_{2.15}Sn_{0.85}S_3$ sample) was collected at room temperature on the endstation CX2 devoted to the high-resolution XRD measurements of MARS (Multi-Analysis On Radioactive Samples) beamline at SOLEIL synchrotron (Saint-Aubin, France). The beamline uses a bending magnet source and the X-rays are monochromatized by a double crystal monochromator (DCM) equipped with a pair of Si(220) crystals. The second crystal is sagittally bent to perform the horizontal beam focusing. Higher harmonics rejection and vertical collimation were achieved using the Pt strip of the two mirrors inserted before and after the DCM with a 3.1 mRad incidence angle. The incident X-ray energy was calibrated using the absorption K-edge of an Y foil (E_0 = 17.038 keV) with a beam sizing about 1000 x 300 μm (H x V) at the sample position. The station is equipped by an angular precision two-circle goniometer for the collection of powder diffraction in Debye-Scherrer geometry. High-resolution data was carried out by the use of a set of 24 detectors equipped with crystal analyzer Ge(111).[28] Sample was finely ground and inserted in a boron glass capillary of diameter 0.3 mm in order to avoid the necessity to correct the data for absorption. The analysis of the diffraction patterns was performed by Rietveld refinement

using the FullProf and WinPlotr software packages.[29,30] Background contribution was estimated manually. Zero-point shift, lattice parameters, peak shape parameters and asymmetry parameters were systematically refined, while fractional atomic coordinates and isotropic displacement parameters (*i.e.* Debye-Waller factors B_{iso}) were refined only for synchrotron XRPD data.

Mössbauer spectroscopy

^{119}Sn Mössbauer spectra were recorded at room temperature (T = 300 K) in transmission geometry with a spectrometer operated in the conventional constant-acceleration mode. Polycrystalline absorber, with natural abundance of ^{119}Sn isotope and areal density of ~15 mg cm^{-2}, was used. The source, kept at room temperature, was $Ba^{119}SnO_3$ with a nominal strength of 10 mCi. A palladium foil of 0.5 mm thickness was used as a critical absorber for tin X-rays. Velocity calibration was performed against a 12 mm-thick α-Fe foil at room temperature. ^{119}Sn isomer shifts (IS) are referred to $BaSnO_3$ at room temperature. Mössbauer spectrum was fitted with a least-squares method program assuming Lorentzian peaks.

Transmission electron microscopy

HAADF-STEM, ED studies, and EDXSTEM were performed on JEM ARM200F cold FEG double aberration-corrected microscope operated at 200 kV and equipped with ORIUS CCD camera, large angle CENTURIO EDX detector, and GIF QUANTUM.TEM specimen was prepared by grinding the material in agate mortar in ethanol and depositing suspension on Ni carbon holey grid.

Precession-assisted electron diffraction tomography

Precession-assisted electron diffraction tomography (PEDT)[31,32] data were obtained using a JEOL F200 (200 kV) transmission electron microscope (TEM) equipped with a Gatan RIO16 camera and a Nanomegas Digistar unit. Samples for TEM investigations were prepared by smoothly crushing powder under ethanol in an agate mortar and depositing drops of the mixture onto a holey carbon membrane supported by a Ni grid. PED patterns were collected on $x = 0.15$ sample with a precession angle of 1.2° and a tilt step of about 1° between each pattern. PEDT data were processed using the programs PETS 2.0[33] and Jana2006.[34] Crystallographic details of data reduction and dynamical refinement are given in Table 1.

EXAFS/XANES

X-ray absorption spectroscopy (XAS) measurements were carried out at room temperature in transmission mode at the K-edge of Cu (8987.96 eV) and Sn (29209.79 eV) at the beamline SAMBA (Spectroscopies Applied to Materials Based on Absorption) at Soleil Synchrotron, France (Proposal 20200538).[35] Radiation coming from a bending magnet source was collimated by a first cylindrical bent mirror onto the Si(220) fixed-exit sagittally-focusing double-crystal monochromator. Harmonic rejection has been performed by the use of a second cylindrical bent mirror that also focused vertically the monochromatic beam.

At the sample position, the spot resulted of 300 × 300 μm^2. Measurements have been collected during continuous monochromator scans monitoring, incident, and transmitted X-ray flux by opportunely filled Oxford ionization chambers.[36] During measurement, a reference sample (a copper or a tin foil) has been simultaneously measured with residual photons of the second ionization chamber for energy calibration. The amount of sample and the thickness of the pellet were optimized in order to have proper XAS signal. The calculated amount of each sample was

grounded, mixed with cellulose, and then compressed to form the pellet. Due to the large difference of X-ray cross section at Sn and Cu K edges, two different samples were prepared for the two energies. The Extended X-ray Absorption Fine Structure (EXAFS) signal treatment was performed according to standard procedures: subtraction of the pre-edge and post-edge backgrounds, edge normalization, extraction of EXAFS signal $\chi(k)$ and its Fourier transformation, which provides a map in the real space of the distribution of the distances R around the absorber atom. Demeter software package was used to perform data treatment and fitting.[37] The model functions were created based on the crystallographic data atom location. For each edge, all the spectrum has been simultaneously fitted, using a single common edge shift. Such approximation has been possible due the strong resemblance of all the spectra and the convention to use exactly the same E_0 during the procedure of EXAFS signal extraction.

X-ray absorption near edge spectroscopy (XANES) calculation has been performed in real space with muffin tin approximation by FEFF code using final state rule and Hedin-Lundqvist exchange correlation potential.[38] For both edge a 10 Å cluster around the absorber has been used.

Electrical and thermal properties measurements

The electrical resistivity (ρ) and Seebeck coefficient (S) were measured simultaneously from $2\times3\times10$ mm^3 ingots, from 300 K up to 700 K using an ULVAC-ZEM3 instrument under partial helium pressure. A NETZSCH LFA-457 apparatus was used for measuring the thermal diffusivity under argon flow. The thermal conductivity (κ) was determined as the product of the geometrical density, the thermal diffusivity, and the theoretical heat capacity using the Dulong−Petit approximation. The lattice contribution to the thermal conductivity (κ_L) was determined by subtracting the estimated electronic component (κ_e) from the measured total thermal conductivity,

κ. The measurement uncertainties are estimated to be 6% for the Seebeck coefficient, 8% for the electrical resistivity, 11% for the thermal conductivity, and 16% for the final dimensionless figure of merit, ZT.[39]

Hall effect measurements over the temperature range of 5 K to 300 K were carried out using a Physical Properties Measurement System (PPMS; Quantum Design) under an applied magnetic field of 9T. Electrical resistivity over the temperature range of 5 K to 300 K was also measured with a PPMS.

An initial assessment of the thermal stability and the reproducibility of the thermoelectric properties of $Cu_5Sn_2S_7$ were carried out through cycling measurements of the electrical transport properties, up to 625 K (**Figure S1**) and 675 K (**Figure S2**). These results show that, up to 625 K, $Cu_5Sn_2S_7$ remains stable with no systematic variation in the performances, all being within the experimental uncertainty. There are very small but systematic variations of the transport coefficient during the stability experiment up to 675 K. Although the overall performance is not significantly affected, the systematic decrease in the Seebeck coefficient may indicate irreversible changes in the materials. The exact nature of these changes will require further experimental investigation.

First principles calculations

All the calculations were computed using the quantum ESPRESSO[40] package as incorporated in the high-throughput infrastructure of AFLOWπ.[41] Optimized norm-conserving PBE pseudopotentials,[42] well converged basis sets corresponding to an energy cutoff of 150 Ry for the wave functions and 600 Ry for the charge density, and ACBN0 functional approach[43] have been used to self-consistently determine the values for the Hubbard corrections for each atomic species of the material. To integrate over the Brillouin zone, a 8 × 4 × 8 (shifted) grid was used for the monoclinic $Cu_5Sn_2S_7$ (space group $C2$).

Transport properties such as, Seebeck coefficient *S*, electrical conductivity σ, and electronic contribution to thermal conductivity κ_e, were computed by solving Boltzmann transport equation within the constant relaxation time and the rigid band approximation as implemented in PAOFLOW.[44] Correction to relaxation time and computation of lattice thermal conductivity κ_l have been performed *a posteriori* comparing experimental electrical resistivity, experimental thermal conductivity, computed electrical conductivity, computed electronic thermal conductivity. Helmholtz free energy were obtained using the calculated phonon density of states employing quasi-harmonic approximation.[45]

3. Results and discussion

3.1. Structure Analysis

3.1.1. X-ray powder diffraction analysis of the system $Cu_{2+x}Sn_{1-x}S_3$

The X-ray powder diffraction (XRPD) patterns recorded on the $Cu_{2+x}Sn_{1-x}S_3$ samples for x = 0, 0.075, and 0.15 (**Fig. 1**), exhibit high intensity diffraction peaks related to the sphalerite structure, characterized by a progressive shifting toward high angles as the Cu/Sn ratio increases. This indicates that the size of the pseudo sphalerite sub-cell decreases as the copper content increases in agreement with the smaller ionic radius of Cu^+ compared to Sn^{4+}. However, low intensity peaks appear, which are different in positions suggesting different orderings of these sphalerite derivatives. Note that the absence of common superstructure diffraction peaks indicates the absence of phase mixture.

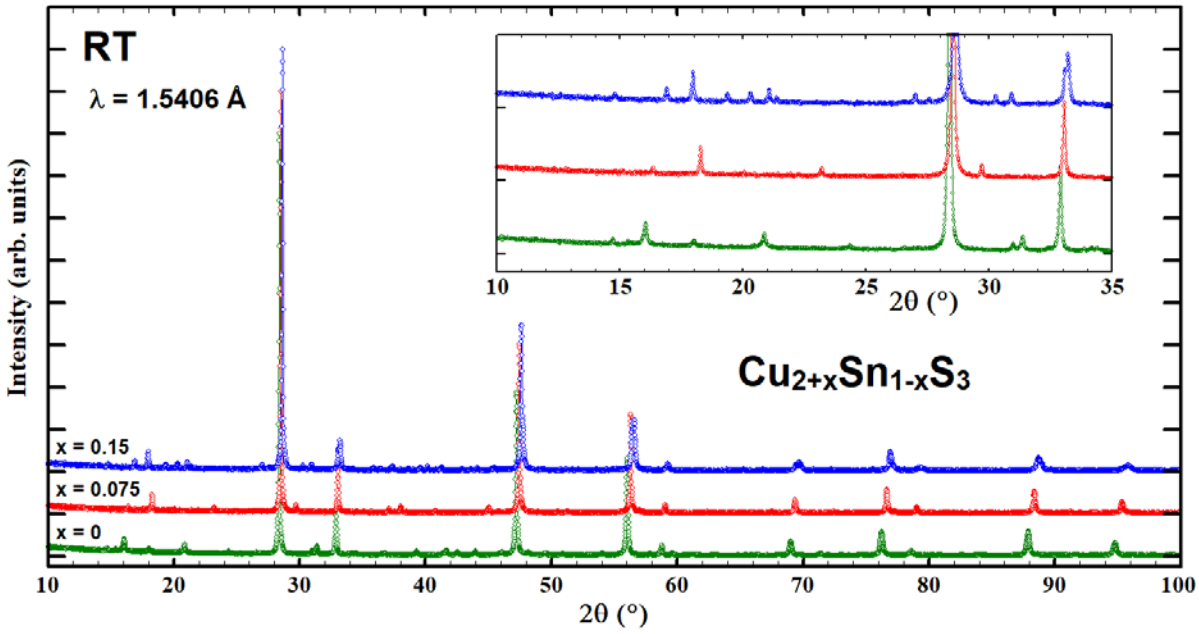

Figure 1. XRPD patterns of Cu_2SnS_3 (green), $Cu_{2.075}Sn_{0.925}S_3$ (red), and $Cu_{2.15}Sn_{0.85}S_3$ (that is $Cu_5Sn_2S_7$, blue) samples.

The XRPD pattern analysis of the $x = 0$ sample confirms the formation of the monoclinic Cu_2SnS_3 mohite phase: Cc, a = 6.656(1) Å, b = 11.525(2) Å, c = 6.658(1) Å, and β = 109.52(1)° (**Fig. S3**). The XRPD pattern of the $x = 0.075$ sample could be indexed in a tetragonal unit cell similar to that of kuramite ($I\bar{4}2m$) in agreement with the observations reported by Deng *et al.* in $Cu_7Sn_3S_{10}$ (x = 0.1).[3] However, while apparent high quality Rietveld refinements are obtained with a kuramite structural model, all the attempts lead to anomalous refined atomic parameters. In particular, the compositional refinements, leading to much lower tin content than that of the nominal composition $Cu_{2.075}Sn_{0.925}S_3$, suggest that the structural model proposed by Deng *et al.*[3] does not fit this composition. Note that Deng *et al.* also mentioned a chemical composition deviation with a much lower refined tin content than that of the nominal composition but decided to overcome this

deviation by fixing the site occupancies in accordance with the nominal composition. A redetermination of the crystal structure of this phase is in progress.

The XRPD pattern analysis of the $x = 0.15$ sample ($Cu_{2.15}Sn_{0.85}S_3$) indicates the formation of a new compound in the ternary system Cu-Sn-S. The splitting of the main diffraction peak at $2\theta = 13.4°$ (*i.e.* corresponding to the reflection 111 in sphalerite structure) in two distinct reflections suggests that the compound crystallizes in a monoclinic unit cell (**Fig. 2**). This is confirmed by the perfect indexing of all diffraction peaks with the refined unit cell parameters a = 12.0580(5) Å, b = 5.4063(2) Å, c = 8.5026(3) Å, and β = 98.163(3)°. The systematic absence of the reflections hkl with $h + k = 2n + 1$ indicates a C-face centered unit cell and the presence of reflections $h0l$ with $l = 2n + 1$ allows to exclude the presence of a c glide mirror (**Fig. 2**). Moreover, the presence of the high intensity diffraction peaks related to the sphalerite structure suggests that a centrosymmetric space group can be excluded. Consequently, the possible space groups are either $C2$ or Cm.

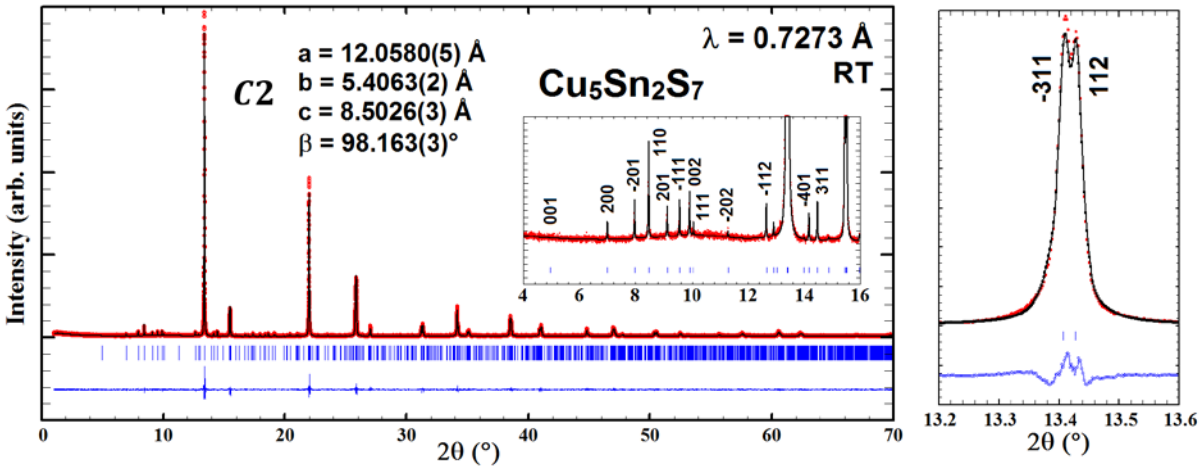

Figure 2. Synchrotron XRPD Rietveld refinement of the $Cu_{2.15}Sn_{0.85}S_3$ sample corresponding to the $Cu_5Sn_2S_7$ phase.

3.1.2. Combined PEDT and synchrotron XRPD refinements of $Cu_5Sn_2S_7$ (x = 0.15) structure

Structure analysis based on precession-assisted electron diffraction tomography (PEDT) was carried out on sub-micrometer single crystals obtained from the same powder sample. First, by examining the reconstructed reciprocal space of several crystals, we can confirm the C-centered monoclinic lattice with possible space groups $C2$, Cm or $C2/m$ (**Fig. 3**). Secondly, symmetry analysis[46] of the structure solution performed using the charge flipping method,[47] indicates the $C2$ as more probable with symmetry agreement factors ranked as follow: 2(0,1,0) = 5.7, m(0,1,0) = 19.7, -1=20.1 and c(0,1,0) = 55.4. From these crystallographic considerations and literature data, the structural model reported by Schäfer *et al.*[24] for $Cu_4NiSi_2S_7$ (space group $C2$) seems well adapted when Ni and Si atoms are replaced by Cu and Sn atoms, respectively. The PEDT study of this compound detailed in supplementary information (**Tables S1, S2**) in combination with the structural refinement indicates that the chemical composition of this ternary compound is $Cu_5Sn_2S_7$. Rietveld refinement of synchrotron XRPD pattern confirms this structural model and the sample purity, with well reproduced intensities of the superstructure diffraction peaks (**Fig. 2**). Crystallographic data of $Cu_5Sn_2S_7$ obtained by Rietveld refinement against the synchrotron XRPD data are gathered in **Table 1**.

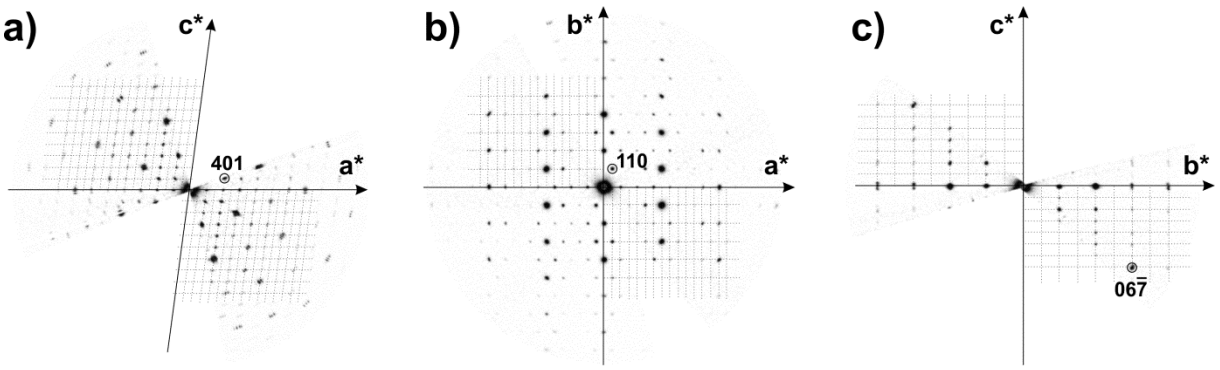

Figure 3. Reciprocal space sections reconstructed from PEDT data for $Cu_5Sn_2S_7$ with: a) *h*0*l*, b) *hk*0 and c) 0*kl*. The dotted lines are used as a guide to the eyes to visualize the reciprocal lattice mesh. The conditions limiting the existence of reflections: *h*0*l*: $h = 2n$, *hk*0: $h+k = 2n$ and 0*kl*: $k = 2n$ are compatible with a C-centering. In a), reflections with indexation *h*0*l* $l = 2n+1$ are clearly visible excluding the presence of a *c* glide mirror.

Table 1. Crystallographic data for $Cu_5Sn_2S_7$ obtained by Rietveld refinement of the room temperature synchrotron XRPD pattern. Origin is fixed to S1. Software used for structure refinement: FullProf [29] and WinPlotr.[30]

$C2$	a = 12.0580(5) Å, b = 5.4063(2) Å, c = 8.5026(3) Å, β = 98.163(3)°				
Atom	Site	x	y	z	SOF
Cu1	2*b*	0	0.771(13)	0.5	1.00
Cu2	4*c*	0.354(2)	0.258(8)	0.073(2)	1.00
Cu3	4*c*	0.214(2)	0.268(11)	0.643(2)	1.00
Sn1	4*c*	0.074(1)	0.276(8)	0.225(1)	1.00
S1	2*a*	0	0	0	1.00
S2	4*c*	0.146(2)	0.002(12)	0.441(3)	1.00
S3	4*c*	0.422(3)	0.026(9)	0.289(3)	1.00
S4	4*c*	0.222(3)	0.523(8)	0.142(3)	1.00

3.1.3. Comparison of the monoclinic Cu_2SnS_3 and $Cu_5Sn_2S_7$ structures

The crystal structure of mohite Cu_2SnS_3 is built up of corner-sharing CuS_4 and SnS_4 tetrahedra (**Fig. 4**) leading to a cationic ordered monoclinic sphalerite framework. A specific structural feature of this sphalerite-derivative framework is related to the existence of zigzag chains of SnS_4 tetrahedra oriented along the *c*-axis, (**Fig. S4a**). These zigzag chains are separated from each other, along both the *a*-axis and *b*-axis, by zigzag chains of CuS_4 tetrahedra oriented along the *c*-axis (**Fig. S4b**). The crystal structure of mohite is completed by chains of the remaining CuS_4 tetrahedra oriented along the [101] direction (**Fig. S4c**).

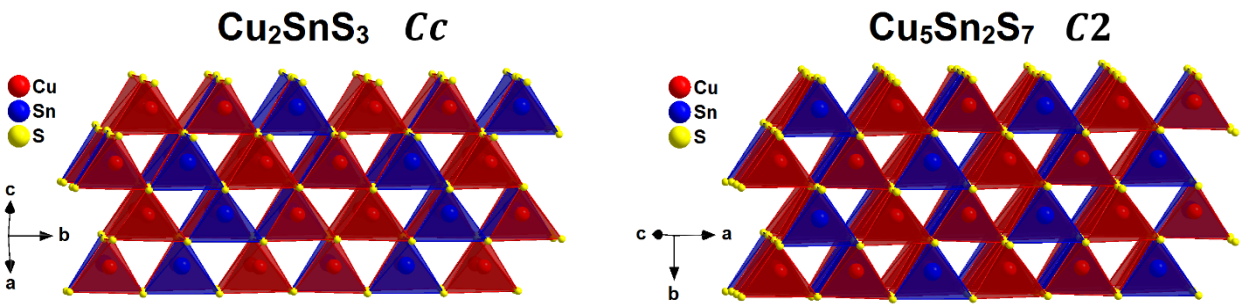

Figure 4. Crystal structure representations of the sphalerite-derivative frameworks encountered in mohite Cu_2SnS_3 (left) and $Cu_5Sn_2S_7$ (right).

Also, the crystal structure of $Cu_5Sn_2S_7$ is built up of corner-sharing CuS_4 and SnS_4 tetrahedral network (**Fig. 4**), corresponding to a cationic ordered monoclinic sphalerite framework. In this monoclinic structure, however, SnS_4 tetrahedra are linked two by two by the S atom in the 2*a* position (*i.e.* S1), leading to the existence of tetrahedral Sn_2S_7 dimers. These dimers form with Cu atoms in the 2*b* position (*i.e.* Cu1) cationic ordered zigzag layers in the (*b*,*c*) plane (**Fig. 5a**). These cationic ordered zigzag layers are separated from each other along the *a*-axis by zigzag layers formed by Cu2 and Cu3 atoms. Within these monoatomic zigzag layers, Cu2 atoms form CuS_4 layers in the (*a*,*b*) plane (**Fig. 5b**) and Cu3 atoms form CuS_4 chains oriented along the *b*-axis (**Fig. 5c**). From a "Cu-S" conductive network point of view, the ordered sphalerite structure of $Cu_5Sn_2S_7$ can be viewed as a tridimensional $[Cu_5S_7]_\infty$ tetrahedral framework forming tunnels running along the *c*-axis where the Sn_2S_7 dimers are located (**Fig. 5d**).

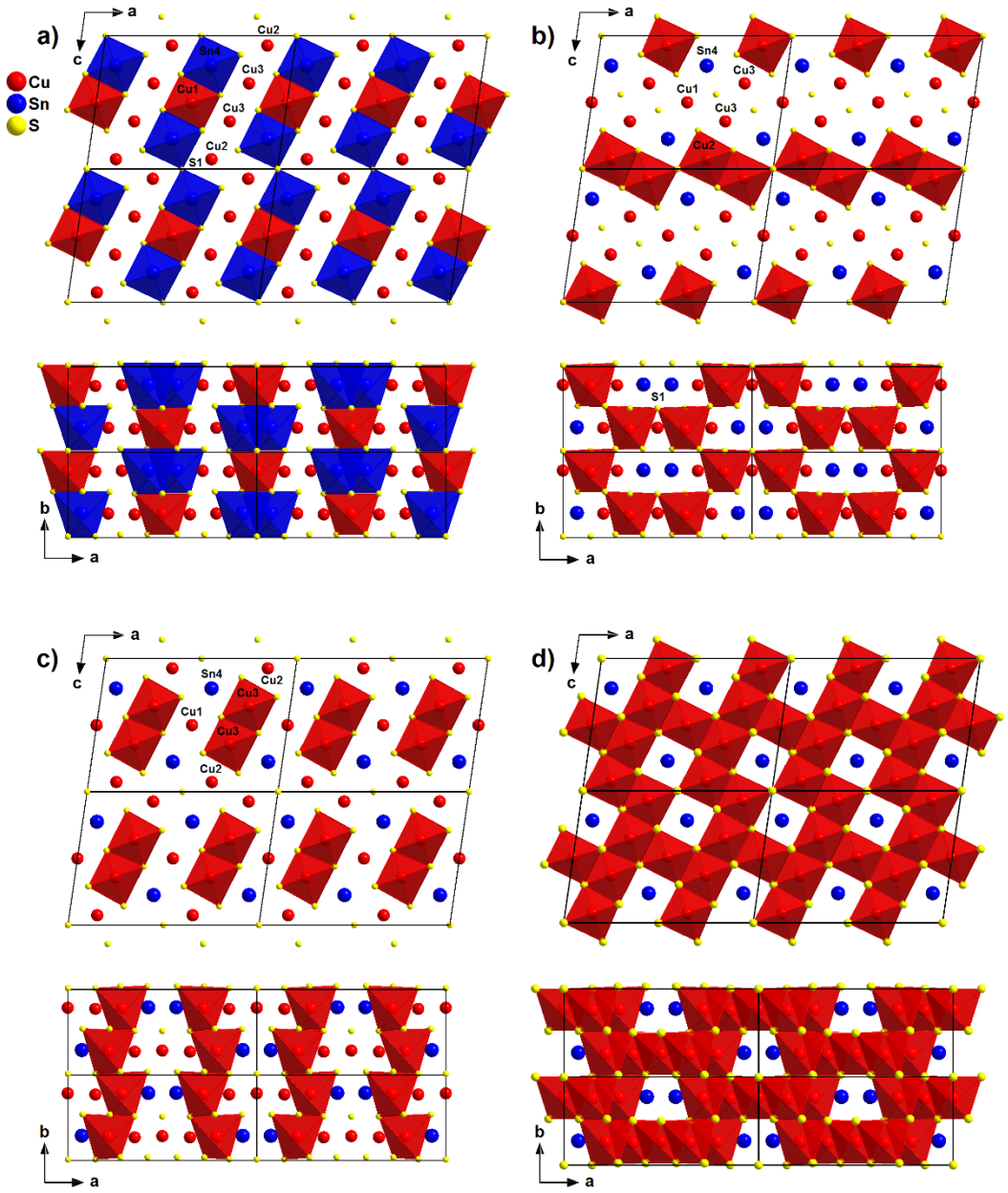

Figure 5. Crystal structure representations along the b-axis (top) and c-axis (bottom) of the different cationic sub-networks (a-d) encountered in the $Cu_5Sn_2S_7$ phase (space group $C2$).

The interatomic distances in $Cu_5Sn_2S_7$, calculated from the Rietveld refinement against the synchrotron XRPD data, are coherent with those generally encountered in copper sulfides with a sphalerite framework, except those between Cu2 and S1 atoms and between Sn4 and S1 atoms,

which are longer than the average Cu-S and Sn-S distances, respectively (**Table 2**). These abnormally long distances for a sphalerite-type framework, both involving S1 atom, suggest a non-negligible role of Sn_2S_7 dimers on the deformation of the "Cu-S" conductive network. This is supported by the average deviation from the ideal tetrahedral angle, more pronounced for Cu1 tetrahedra (Δ_{ave} = 3.65°), which is directly linked to the Sn_2S_7 dimers, than for Cu3 (Δ_{ave} = 1.95°) and Cu2 (Δ_{ave} = 1.34°) tetrahedra. Moreover, Rietveld refinement shows that the average deviation from the ideal angle in the SnS_4 tetrahedra is equivalent in $Cu_5Sn_2S_7$ (Δ_{ave} = 2.29°) and Cu_2SnS_3 (Δ_{ave} = 2.48°, calculated from data reported by Onoda *et al.*[18]). However, in Cu_2SnS_3 the maximum deviations are much higher (-6.4°/+3.7°) than those observed in $Cu_5Sn_2S_7$ (-4.0°/+2.5°) explaining the larger Mössbauer ΔE_Q value of 1.02 mm s^{-1} (see section 3.1.5) measured in Cu_2SnS_3 compared to that of 0.77 mm s^{-1} measured in $Cu_5Sn_2S_7$, as well as the lower mean square relative displacements at the Sn site refined from EXAFS data (see section 3.1.7) for $Cu_5Sn_2S_7$ compared to Cu_2SnS_3. Note that in both crystal structures, Sn atoms are located on a site of local symmetry *1*. Thus, the two monoclinic sulfides Cu_2SnS_3 (mohite) and $Cu_5Sn_2S_7$, corresponding to $x = 0$ and $x = 0.148$ (refined composition) respectively, are highly ordered and the nature of their cationic ordering in the sphalerite framework is very sensitive to the Sn content. One indeed observes the formation of $[SnS_3]_\infty$ zigzag chains of corner-sharing SnS_4 tetrahedra in Cu_2SnS_3 (mohite Cc structure), whereas Sn_2S_7 dimers are observed in $Cu_5Sn_2S_7$ ($C2$ structure).

Table 2. Interatomic distances (Å) and bond angles (°) in $Cu_5Sn_2S_7$ (space group $C2$) from Rietveld refinement of the room temperature synchrotron XRPD pattern.

Cu1-S2 ×2	2.272	S2-Cu1-S2	113.31	S2-Cu3-S2	108.25
Cu1-S3 ×2	2.319	S2-Cu1-S3 ×2	104.06	S2-Cu3-S3	109.07
Cu2-S1	2.349	S2-Cu1-S3 ×2	112.64	S2-Cu3-S3	112.32
Cu2-S3	2.277	S3-Cu1-S3	110.34	S2-Cu3-S4	106.09
Cu2-S4	2.277	S1-Cu2-S3	108.76	S2-Cu3-S4	112.49
Cu2-S4	2.308	S1-Cu2-S4	107.16	S3-Cu3-S4	108.65
Cu3-S2	2.297	S1-Cu2-S4	108.89	S1-Sn4-S2	105.48
Cu3-S2	2.303	S3-Cu2-S4	108.99	S1-Sn4-S3	108.01
Cu3-S3	2.288	S3-Cu2-S4	113.13	S1-Sn4-S4	107.88
Cu3-S4	2.304	S4-Cu2-S4	109.74	S2-Sn4-S3	111.99
$\overline{d_{Cu-S}}$	2.299			S2-Sn4-S4	111.12
Sn4-S1	2.489			S3-Sn4-S4	112.01
Sn4-S2	2.423				
Sn4-S3	2.402				
Sn4-S4	2.412				
$\overline{d_{Sn-S}}$	2.432				

The structural evolution of the system $Cu_{2+x}Sn_{1-x}S_3$ shows a very remarkable feature: although the three compositions exhibit the same sphalerite sub-lattice, the variation in the cationic composition does not allow any continuous solid solution corresponding to a statistic distribution of the Sn^{4+} and Cu^{+} cations in the tetrahedral sites to be obtained. In other words, two ordered sphalerite structures are formed for $x = 0$ and $x = 0.15$ respectively, which are "immiscible" in spite of their close structural relationships and compositions. Moreover, the intermediate $x = 0.075$ composition does not correspond to a mixture of these two ordered sphalerite structures, but to a single phase whose unknown crystal structure is also a derivative of the sphalerite and might be partially ordered/disordered. This behavior can be explained by the fact that the size difference between the Sn^{4+} and Cu^{+} cations, though rather small, governs the matching of the CuS_4 and SnS_4 tetrahedra in the sphalerite framework and consequently their mode of ordering in those sphalerite-type structures. The comparison of the Sn-S distances ranging from 2.40 to 2.49 Å with the Cu-S

distances ranging from 2.29 to 2.35 Å in $Cu_5Sn_2S_7$ (**Table 2**) clearly suggests that the mode of cationic ordering is highly sensitive to the size difference between Sn^{4+} and Cu^{+} cations.

3.1.4. Transmission Electron Microscopy: ED, EDX and HAADF study of $Cu_5Sn_2S_7$ (x = 0.15)

In order to confirm the purity of the $Cu_5Sn_2S_7$ sample determined by synchrotron XRPD and to further investigate the homogeneity of the chemical composition and structure at the atomic scale, transmission electron microscopy (TEM) analyses were performed. Electron diffraction (ED) and EDX elemental mapping were used to confirm the crystal structure of $Cu_5Sn_2S_7$ in connection with its chemical composition. ED patterns collected for the main zones (**Fig. S5a**) can be fully indexed based on the monoclinic $C2$ structure (see **Table 1**). No superstructure spots have been observed. EDX elemental mapping (**Fig. S5b**) shows a quite homogeneous distribution of all the elements and gives the following atomic ratio Cu/Sn/S=38.3/16.24/45.4 (at. %) which is close to the nominal composition.

High angle annular dark field scanning TEM (HAADF-STEM) images of crystallites along two most informative zone axis ([010] and [110]) demonstrate the good crystallinity of the sample and the fair correspondence with the monoclinic structure determined by PEDT and synchrotron XRPD (**Fig. 6**). The images demonstrate a uniform contrast free from any modulations and defects in accordance to the structural model. HAADF-STEM image simulation using this structure model shows good agreement with experimental images (**Fig. 6 inserts**). ED and HAADF-STEM studies revealed numerous twinning phenomena, which are visible along the [010] and [110] zone axes. **Fig. 6e** shows the HAADF-STEM image of one of the examples of the {110} twinning viewed along the [110] direction. The twin boundary is parallel to <110> planes. On the basis of the

HAADF-STEM image, a structural model for the twin boundary is presented in **Fig. 6f** (bottom panel).

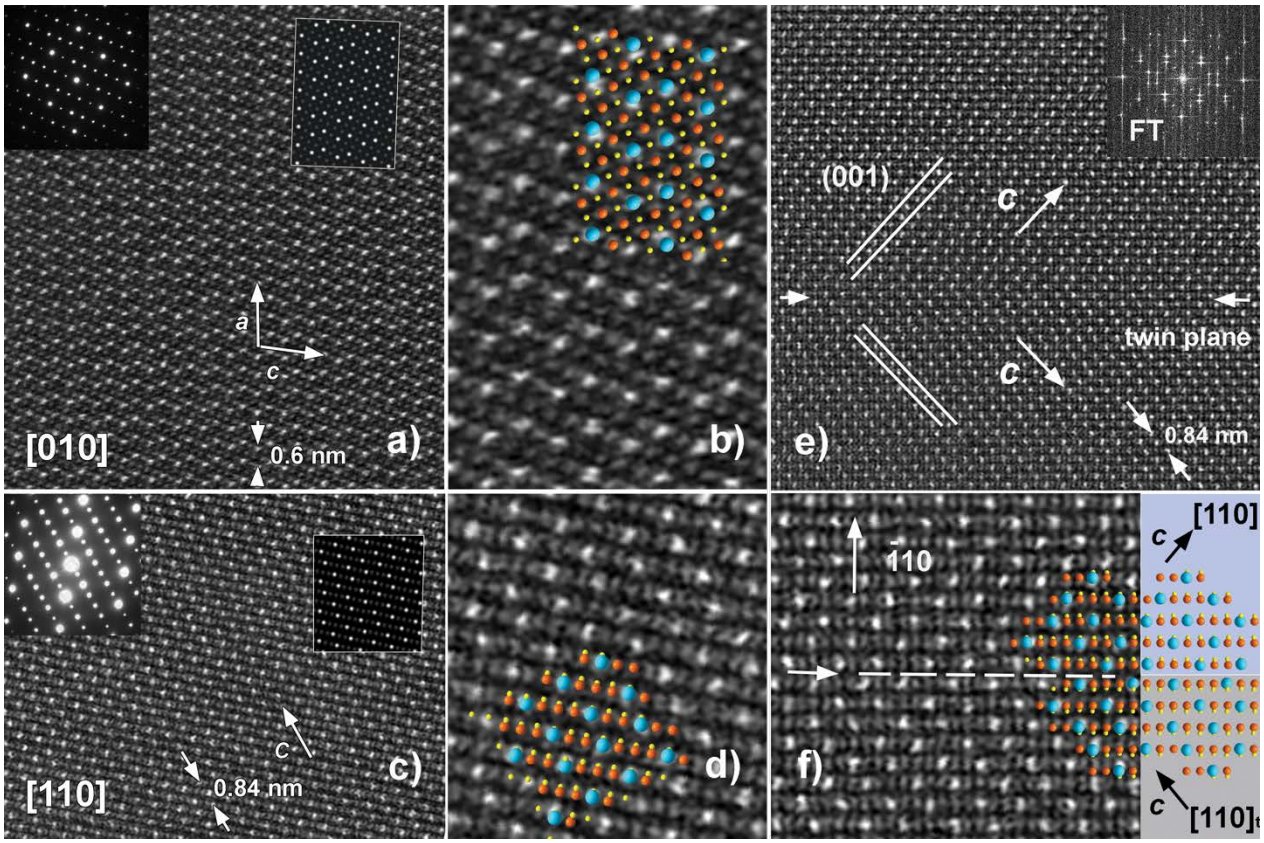

Figure 6. HAADF-STEM images for two main zone axis [010] (a, b) and [110] (c, d) and corresponding ED patterns. The simulated HAADF-STEM images based on the $C2$ monoclinic structure determined by PEDT and synchrotron XRPD are given as insets. The magnified images with overlaid color structural models are present in b) and d) panel (Sn-blue, Cu-orange and S-yellow). [110] HAADF-STEM image of the twinning region and corresponding FT pattern (e). The panel f) shows a magnified twin boundary and the corresponding structural model (Sn-blue, Cu-orange and S-yellow). The twin plane is indicated by white arrows and dashed line.

3.1.5. ^{119}Sn Mössbauer spectroscopy

In order to shed light on the influence of the Cu/Sn ratio on the local environment of tin atoms in the $Cu_{2+x}Sn_{1-x}S_3$ series, ^{119}Sn Mössbauer spectra were recorded at room temperature for the three samples: $x = 0$, $x = 0.075$, and $x = 0.15$. The least-squares fits of the experimental data are shown in **Fig. 7** and the corresponding hyperfine parameters are given in **Table 3**.

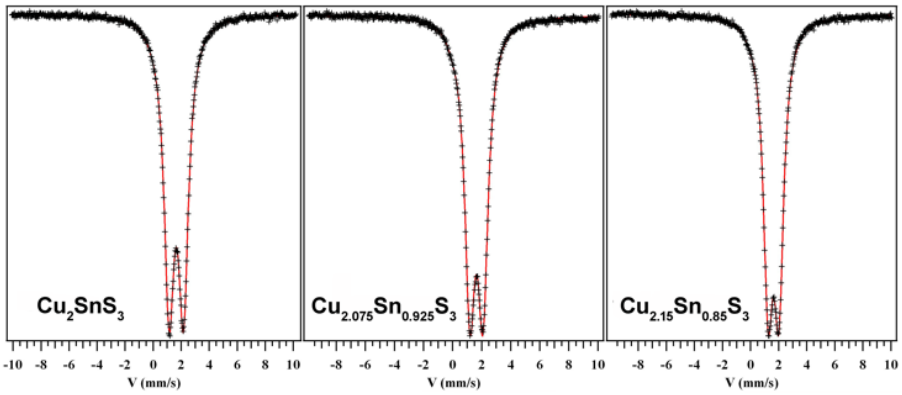

Figure 7. Room temperature ^{119}Sn Mössbauer spectra of the $Cu_{2+x}Sn_{1-x}S_3$ samples: (left) $x = 0$, mohite Cu_2SnS_3 phase (space group Cc); (middle) $x = 0.075$; (right) $x = 0.15$, $Cu_5Sn_2S_7$ phase (space group $C2$). Experimental data and least-squares fits are represented by black crosses and red lines, respectively.

First, fits of the ^{119}Sn Mössbauer spectrum evidence a doublet centered at 1.54 mm s^{-1} (with respect to $BaSnO_3$ at room temperature) for the three samples. This indicates that Sn atoms are in their +IV oxidation state[49] and in tetrahedral environment of sulfur.[50–53] Additionally, the fact that this value is unchanged indicates that the valence electron density at the tin nucleus is equivalent,[54,55] whatever the sample composition. This result highlights that Cu for Sn substitution in the $Cu_{2+x}Sn_{1-x}S_3$ series does not influence the oxidation state of Sn atoms. The full width at half maximum (FWHM or Γ) of the peaks is similar for the three samples and is equivalent to values observed in well-ordered sphalerite framework compounds.[53–55] Third, the quadrupole splitting (ΔE_Q)

decreases with the tin content from 1.02 mm s^{-1} for Cu_2SnS_3 to 0.77 mm s^{-1} for $Cu_5Sn_2S_7$ (**Table 3**). As ΔE_Q value reflects the deviation from a spherical symmetry of the charge distribution at the nucleus, it suggests that the environment of the Sn^{4+} cations is less anisotropic in $Cu_5Sn_2S_7$ than in Cu_2SnS_3. This point will be discussed in detail in the following sections. On the other hand, the ΔE_Q value of 0.90 mm s^{-1} for the $Cu_{2.075}Sn_{0.925}S_3$ sample suggests a structural disordering instead of a distorted environment. It strongly supports our preliminary XRPD study suggesting that the crystal structure of this intermediate phase merits to be reinvestigated.

Table 3. ^{119}Sn hyperfine parameters of the three $Cu_{2+x}Sn_{1-x}S_3$ samples at 300 K: isomer shift (IS), quadrupole splitting (ΔE_Q) and FWHM (Γ). IS values are given with respect to $BaSnO_3$ at room temperature.

$Cu_{2+x}Sn_{1-x}S_3$	IS mm s^{-1} (± 0.01)	ΔE_Q mm s^{-1} (± 0.01)	Γ mm s^{-1} (± 0.01)
x = 0, Cu_2SnS_3	1.55	1.02	0.87
x = 0.075	1.54	0.90	0.82
x = 0.15, $Cu_5Sn_2S_7$	1.54	0.77	0.83

3.1.6. Formation energies computed from first principles calculations

Assuming Cu^+, Sn^{4+}, and S^{2-}, charge compensation indicates that Cu_2SnS_3 is fully compensated while $Cu_5Sn_2S_7$ has two holes per unit cell. Formation energies (**Table 4**) computed from first principles indicate that the $C2$ $Cu_5Sn_2S_7$ and the Cc Cu_2SnS_3 at zero temperature are equivalent within 1 meV. By including the vibrational effects, $C2$ phase gains relative stability with temperature up to 15 meV at 700 K. Within the uncertainty of the structural model due to partial occupations, the tetragonal and cubic phases are about 120-130 meV higher in formation energy. We conjecture that the replacement of Sn with Cu drives the formation of the new monoclinic phase by injecting holes into the system and introducing local stresses associated with Sn-Cu size

mismatch. These trigger interactions, which favor the formation and long-range ordering of "dimers" of Sn centered tetrahedra.

Table 4. Formation energies per atom with respect to elemental solids. The monoclinic Cc Cu_2SnS_3 (x = 0, underlined) is the ground state. At x = 0.15, the most favored structure is the monoclinic $C2$ $Cu_5Sn_2S_7$ (underlined). The values for other concentrations were computed using a 64 atoms supercell to model the Sn-Cu disorder. All the disordered phases are less favored.

x	Formation energy [eV]				
0.00	<u>-0.327</u>	-0.226)	-0.193	-0.187	-0.178
0.083	-0.212	-0.212	-0.212	--	--
0.150	<u>-0.341</u>	--	--	--	--
0.167	-0.198	-0.197	-0.198	--	
0.750	-0.183	-0.182	-0.182	-0.182	--

3.1.7. X-ray Absorption Near Edge Spectroscopy/Extended X-ray Absorption Fine Structure analysis

Figure 8 shows XANES spectra for Cu_2SnS_3, $Cu_{2.075}Sn_{0.925}S_3$ and $Cu_{2.15}Sn_{0.85}S_3$ samples with respect to standard compounds Cu metal, Cu_2S and $Cu(NH_3)_4^{2+}$. The spectral shape for each sample is relatively similar, confirming a similar local structure (sphalerite framework) for all the samples with the position of the edges mainly suggesting an oxidation state 1+ for copper (**Figure 8a**). Among the small differences between the samples, we could notice for $Cu_{2.075}Sn_{0.925}S_3$ and $Cu_{2.15}Sn_{0.85}S_3$ samples a slight blue-shift of the edge with respect to Cu_2SnS_3 (red arrow in **Figure 8a**) and the appearance of a small contribution at around 8977 eV (blue arrow in **Figure 8a**). Both features could be attributed to the presence of a small contribution of Cu^{2+}, in particular the peak at 8977 eV is assigned to quadrupolar transition of 1s $\rightarrow$ 3d Cu level (**Figure S6**). Note that in Cu^+ 3d levels are normally fully occupied and, consequently, not available for the transition. Such

assignment is confirmed by the presence of similar pre-edge peak in the model compound $Cu(NH_3)_4^{2+}$ (blue arrow in **Figure 8a**) or in CuS.[56]

The good agreement between XANES simulation and experimental spectra (**Figure S7**) shows that the crystal structure is representative also of the actual local structure around the copper atoms. Moreover, it is clear by increasing the size of used cluster during simulations that the several features on the spectra result from long range interactions.

The XANES spectra at Sn K-edge contain comparatively fewer features (**Figure 8b**). Indeed, the spectra are affected by the large core hole lifetime of 1s level, ~ 6 eV, that prevents fine feature to be present. Despite this lack in resolution, it is clear that the decreasing content of Sn does not affect the XANES spectra that are basically superimposed for all the three samples, suggesting no variation in the oxidation state. This result is in fair agreement with ^{119}Sn Mössbauer data.

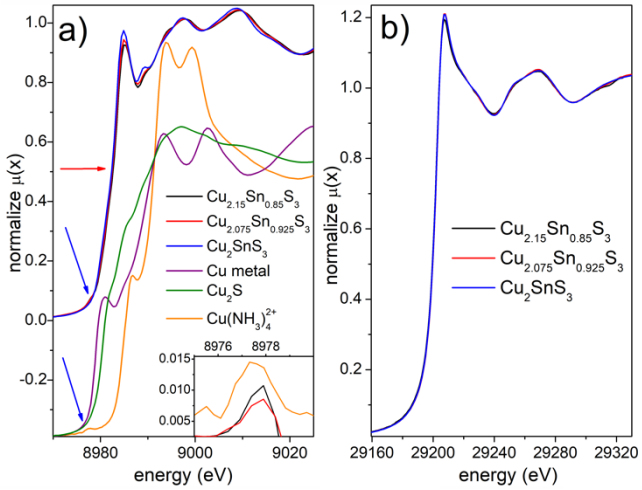

Figure 8. XANES spectra: a) Cu K-edge and b) Sn K-edge, for Cu_2SnS_3 (blue curve), $Cu_{2.075}Sn_{0.925}S_3$ (red curve) and $Cu_{2.15}Sn_{0.85}S_3$ (black curve). The inset in a) focuses on a region around the quadrupolar 1s→3d transition peak. In order to isolate such transition from the background, the spectrum of Cu_2SnS_3 have been subtracted from $Cu_{2.15}Sn_{0.85}S_3$ (black curve) and

$Cu_{2.075}Sn_{0.925}S_3$ (red curve) spectra, while for the spectra of $Cu(NH_3)_4^{2+}$ a spline function has been used.

The EXAFS signals for Cu and Sn K edges and results of its analysis are shown in **Figure 9**. All the data have good statistics allowing significant fit with good agreement factors (**Table 5**). As can be observed, the signals are dominated by a single frequency attributed to the single scattering of sulfur atoms in the first coordination shell. A small signal around 3.7 Å (not phase corrected) is present for Sn signal attributed to the contributions of the second shell, which has not been fitted due to numerous different components composing the signals. Second shell contributions are absent in the Cu signals reflecting the large heterogeneity of contributions due to the presence of different crystallographic sites for Cu atoms.

Although the spectra results are very similar, differences are just above the estimation of standard deviation (**Table 5**), it should be noticed that all refined parameters showed a strong correlation with the Sn concentration in the samples. For both edges, the Cu-S and Sn-S bonds lengths decrease with the increase in Cu content. In the case of copper, this effect could be explained by a partial oxidation, as noticed by the XANES analysis. Moreover, the mean square relative displacements refined at Sn K edge decrease with increasing Cu content (**Table 5**), reflecting a decrease of disorder at the tin site from Cu_2SnS_3 to $Cu_5Sn_2S_7$, in agreement with ^{119}Sn Mössbauer results.

Finally, the fitted distances are in good general agreement with diffraction data, although a direct comparison should be taken with caution due to the different nature of the two techniques (local order vs. long range order). Both distances found by EXAFS or XRPD are in reasonable agreement with the expected values calculated by the bond valence sum method,[57] although Sn-S bond lengths are slightly longer than expected.

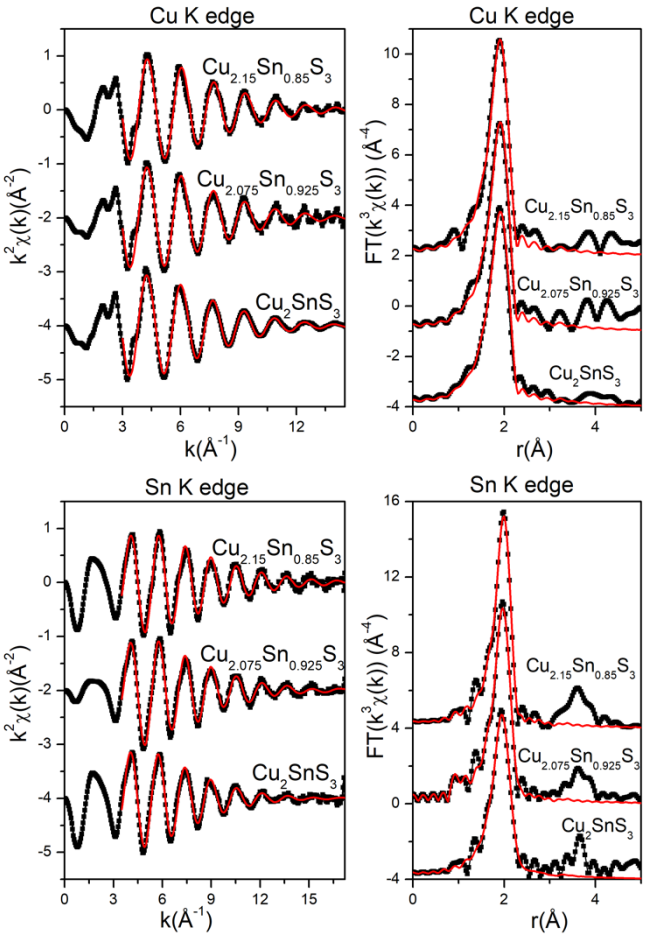

Figure 9. Experimental EXAFS data (black curve with scatter) and fit (red curve) for samples Cu_2SnS_3, $Cu_{2.075}Sn_{0.925}S_3$, and $Cu_{2.15}Sn_{0.85}S_3$ at the Cu (top part) and Sn (bottom part) K-edges. Unfiltered $\chi(k)k^2$ signals and its magnitude of Fourier transformation (FT) are shown in the right and left side respectively.

Table 5. Summary of the parameters obtained by combined least square refinements of χ(k) measured at the Sn and Cu K-edges for samples Cu_2SnS_3, $Cu_{2.075}Sn_{0.925}S_3$ and $Cu_{2.15}Sn_{0.85}S_3$. N, S_0^2, R, σ^2 and ΔE_0 correspond to degeneracy, passive electron reduction function, distance, mean square relative displacements and shift in the edge energy, respectively.

Sn K edge	k_{range}= 3.5-18.3 Å^{-1}, R_{range}= 1.15 - 2.7Å, fitted in R space
Cu K edge	k_{range}= 3.5-14.5 Å^{-1}, R_{range}= 1.1 - 3Å, fitted in R space

Sample	N	S_0^2	R (Å)	σ^2 (Å^2)	ΔE_0 (eV)	R-factor k^2
Cu_2SnS_3_Sn	4	1.26(7)	2.428(4)	0.0079(7)	5.3(4)	0.00910
$Cu_{2.075}Sn_{0.925}S_3$_Sn	4	1.22(7)	2.421(3)	0.0064(6)	5.3(4)	0.00789
$Cu_{2.15}Sn_{0.85}S_3$_Sn	4	1.1(1)	2.418(4)	0.0051(9)	5.3(4)	0.00694
Cu_2SnS_3_Cu	4	0.76(3)	2.303(4)	0.0078(5)	3.0(5)	0.00813
$Cu_{2.075}Sn_{0.925}S_3$_Cu	4	0.7(1)	2.296(8)	0.007(2)	3.0(5)	0.01083
$Cu_{2.15}Sn_{0.85}S_3$_Cu	4	0.72(8)	2.290(6)	0.006(1)	3.0(5)	0.01465

3.2. Transport properties and DFT calculations

Figures 10a and **10b** show the temperature-dependent electrical resistivity (ρ) and Seebeck coefficient (S), respectively, of the $Cu_{2+x}Sn_{1-x}S_3$ series from room temperature to 700 K. The very high ρ and positive S values, that reach ~1800 mΩ cm and 740 μV K^{-1} at 300 K, respectively, indicate that pristine Cu_2SnS_3 behaves as a lightly-doped, nearly-intrinsic *p*-type semiconductor. This semiconducting nature is consistent with the electronic band structure of the Cc phase pointing to a relatively large electronic band gap E_g of 0.8 eV and a valence band dominated by the hybridization of the Cu *d*-states with the S *p*-states with a negligible contribution from the Sn states.[27] The theoretical value of E_g is in good agreement with the value of 0.82 eV inferred from the Goldsmid-Sharp relation $E_g = 2eS_{max}T_{max}$, where e is the elementary charge and $S_{max} = 780$ μV K^{-1} is the maximum S value achieved at $T_{max} = 525$ K. Both values are in reasonable agreement with the value of 0.95 eV inferred experimentally from optical absorption spectroscopy on polycrystalline Cu_2SnS_3 samples.[19]

Varying the Cu-to-Sn ratio results in a significant decrease in ρ and S, which both increase with increasing temperature indicative of degenerate p-type semiconducting behaviors. The $C2$ $Cu_5Sn_2S_7$ phase (x = 0.15) contains two holes per unit cell (Z = 2), leading to a degenerate semiconductor (**Fig. 11**) with the Fermi level 0.38 eV below the top of S-Cu manifold. Sn states contribute to the highly dispersive unoccupied band starting at 0.36 eV above the top of the S-Cu valence manifold.

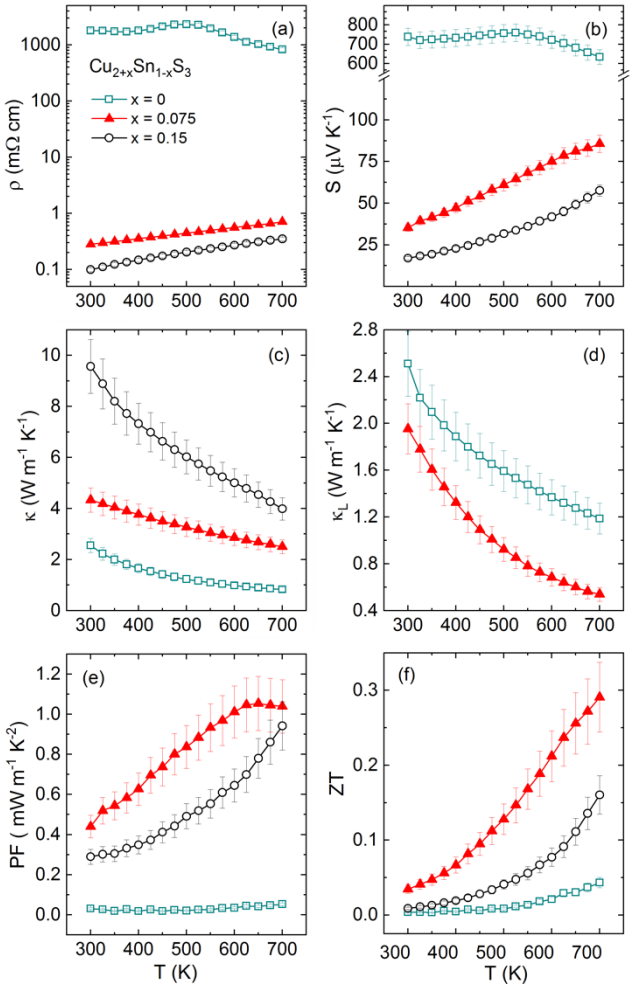

Figure 10. Temperature dependence of the a) electrical resistivity (ρ), b) Seebeck coefficient (S), c) thermal conductivity (κ), d) lattice thermal conductivity (κ_L), e) power factor (PF), and f) dimensionless figure of merit ZT for the $Cu_{2+x}Sn_{1-x}S_3$ series.

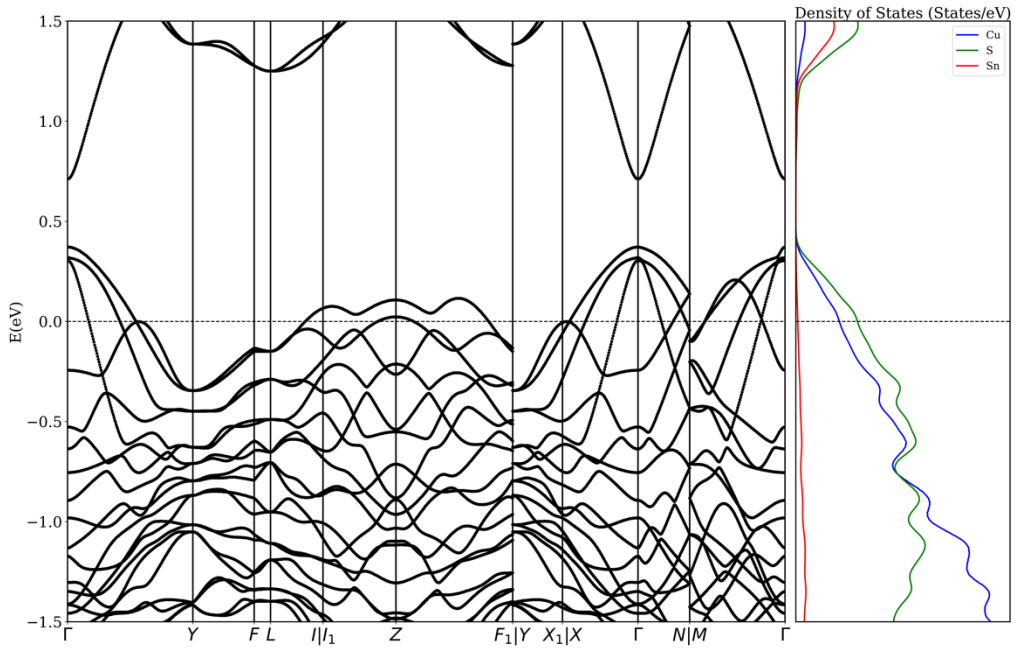

Figure 11. Electronic band structure of monoclinic $C2$ $Cu_5Sn_2S_7$ computed within the ACBN0 approach.

The significant decrease in electrical resistivity with increasing Cu over-stoichiometry, from 1800 mΩ cm for x = 0.00 to much lower values ranging from 0.1 mΩ cm at 300 K up to about 0.35 mΩ cm at 700 K in the x = 0.15 sample ($Cu_5Sn_2S_7$), is consistent with the increased metallicity. Likewise, S increases from 35 μV K^{-1} at 300 K to 85 μV K^{-1} at 700 K for $Cu_{2.075}Sn_{0.925}S_3$ and from 15 μV K^{-1} at 300 K to 58 μV K^{-1} at 700 K for $Cu_{2.15}Sn_{0.85}S_3$. Both samples exhibit S values that are an order of magnitude lower than those of pristine Cu_2SnS_3, due to their degenerate semiconducting behavior. First principles calculations of the Seebeck coefficient within the constant scattering approximation are in fair agreement with the experimental data (**Figure S8**). We have fitted the temperature dependence of the scattering time obtaining a variation from 0.8 10^{-14} s at 300K to 2.9 10^{-14} s at 800K.

With two holes per unit cell in the $C2$ phase, the theoretical hole concentration (p_H) is expected to be around 4×10^{21} cm^{-3}. In agreement with these considerations, experimental values of p_H increase from approximately 2.2×10^{17} cm^{-3} in pristine Cu_2SnS_3 to 4.70×10^{21} cm^{-3} for x = 0.075 and to 5.75×10^{21} cm^{-3} for x = 0.15 at 300 K.

The weak temperature dependence of p_H in the x = 0.075 and x = 0.15 samples upon cooling to 5 K is consistent with their degenerate behaviors (**Figure S9**). The hole concentrations achieved in the present series are similar to those measured in the sulfur-based compounds $Cu_7Sn_3S_{10}$ (2.7×10^{21} cm^{-3}), $Cu_{2.08}Sn_{0.92}S_3$ (~ 2.3×10^{21} cm^{-3}) or in the Se analogue $Cu_5Sn_2Se_7$ (~ 3.1×10^{21} cm^{-3}).[3,20,25] Increasing the Cu content to x = 0.15, twice as high as in $Cu_{2.075}Sn_{0.925}S_3$, does not lead to a similar increase in p_H because of the influence of the crystal structure modifications.

The key role played by the lattice symmetry and crystal structure on the electronic properties of the x = 0.075 and 0.15 samples is highlighted by the distinct temperature-dependent behaviors and magnitudes of the Hall mobility μ_H, shown in **Figure S10**. Despite the higher hole concentration in the x = 0.15 sample compared to the x = 0.075 sample, μ_H increases from 4.6 cm^2 V^{-1} s^{-1} for x = 0.075 to 11.7 cm^2 V^{-1} s^{-1} for x = 0.15 at 300 K. Upon cooling, μ_H increases for both compounds to reach 8.8 cm^2 V^{-1} s^{-1} and 140 cm^2 V^{-1} s^{-1} at 5 K for the x = 0.075 and 0.15 sample, respectively. While both samples show nearly temperature-independent μ_H values below about 30 K, suggesting neutral impurity scattering as the dominant scattering mechanism, $\mu_H(T)$ follows distinct dependences above this temperature. For the x = 0.15 sample, $\mu_H(T)$ evolves according to a $T^{-3/2}$ law characteristic of acoustic phonon scattering. In contrast, the weaker decrease in $\mu_H(T)$ for x = 0.075 roughly follows a $T^{-1/2}$ dependence indicative of alloy scattering, observed, for instance, in solid solutions or strongly off-stoichiometric compounds.[58,59] Thus, these results indicate a higher level of atomic disorder in the x = 0.075 sample with respect to the x = 0.15 sample. Of note,

because of the comparable grain size (500 nm-1 µm, **Figure S11**) and relative density (91-92%) of the SPS pellets, this variation in the prevailing scattering mechanism is not due to microstructural effects and can be thus considered as intrinsic to both compounds. Although they exhibit the same sphalerite sublattice, the cationic ordering substantially differs, leading to two different Cu-S frameworks. Calculations of the real-space partial charge density distribution performed for Cu_2SnS_3 have indicated that the three-dimensional [-Cu-S-Cu-] network forms an antibonding conductive framework that favors hole transport and helps to maintain relatively high mobility values.[27] The low mobility values of the x = 0.075 sample and their temperature dependence suggest a more disordered conductive network formed by CuS_4 tetrahedra due to cationic mixed occupancies. In contrast, a well-ordered crystal structure is observed in the monoclinic $C2$ phase ($Cu_5Sn_2S_7$, x = 0.15) with Cu solely occupying three independent crystallographic sites (2*b*, 4*c* and 4*c*), which likely favors a similar highly-conductive framework and explains the conventional behavior of $\mu_H(T)$ observed in most of thermoelectric materials used above room temperature. In addition, electronic band structure calculations show that, in the proximity of the Fermi energy, the electronic levels tend to exhibit quasi-linear dispersion (**Figure 11**) leading to low average effective masses. Indeed, analyzing the electronic band structure in a window of 600 eV centered on the Fermi level, we have found 31 k-points corresponding to $\nabla_k E_n(\boldsymbol{k}) = \mathbf{0}$ (interestingly many saddle points), averaging out across the Brillouin zone gives an DOS effective mass of about 0.6 m_0 which also correspond to the effective mass at the top of the valence manifold at Γ. The low m^*_{DOS} is consistent with the high hole mobility of the conductive network. We further note that this value is significantly lower from those inferred from a single isotropic parabolic band model (SPB) with acoustic phonon scattering as the dominant scattering mechanism that yields large values of 5.1 m_0 and 2.4 m_0 for the x = 0.075 and 0.15 samples, respectively. While similar to those determined in

a prior theoretical study,[27] the significant difference with the value computed herein reflects the limit of the SPB model in describing transport in multiband systems and in capturing effects such as high alloy scattering potential.

The temperature dependence of the power factor $PF = \alpha^2/\rho$ is shown in **Figure 10e** for the three $Cu_{2+x}Sn_{1-x}S_3$ compositions. The highest value is obtained for $x = 0.075$ over the whole temperature, with values increasing from 0.45 mW m^{-1} K^{-2} at 300 K to 1.03 mW m^{-1} K^{-2} at 700 K. These high values may stem from sharp features in the density of states due to chemical disorder. The maximum value of 1.05 W m^{-1} K^{-2} achieved at 650 K is comparable to that obtained in Zn- and Co-doped Cu_2SnS_3, and only slightly below that achieved in $Cu_7Sn_3S_{10}$.[1,3,17] In contrast, the highly-metallic monoclinic phase, x = 0.15, exhibits a combination of low electrical resistivity and Seebeck coefficient, resulting in moderate power factors that range between 0.3 mW m^{-1} K^{-2} at 300 K and 0.94 mW m^{-1} K^{-2} at 700 K.

Figure 10c shows the temperature dependence of the total thermal conductivity κ for the $Cu_{2+x}Sn_{1-x}S_3$ series. At room temperature, the pristine phase Cu_2SnS_3 exhibits a relatively low κ value of ~ 2.5 W m^{-1} K^{-1}, which is consistent with the value of 2.4 W m^{-1} K^{-1} measured by Shen *et al.* in the series $Cu_2Sn_{1-x}Zn_xS_3$.[1] For the Cu-rich samples, κ increases gradually with increasing the Cu content to reach 4.3 W m^{-1} K^{-1} and 9.5 W m^{-1} K^{-1} at 300 K for the x = 0.075 and x = 0.15 samples, respectively. Regardless of the chemical composition, κ decreases upon heating to 0.8, 2.5 and 3.8 W m^{-1} K^{-1} at 700 K for the x = 0.0, 0.075 and x = 0.15 samples, respectively.

The κ values of Cu_2SnS_3 mainly reflect the lattice contribution κ_L due to its nearly intrinsic semiconducting nature that gives rise to high ρ values and hence, to a negligible electronic contribution κ_e according to the Wiedemann-Franz law $\kappa_e = LT/\rho$, where L is the Lorenz number.

In contrast, the significantly higher values of the two Cu-rich samples are due to their degenerate semiconducting behavior that induces higher electronic contributions.

In order to dissociate the lattice and electronic contributions from the total thermal conductivity, the Wiedemann-Franz law was applied by taking into account the temperature dependence of the Lorenz number using a single-parabolic-band model with acoustic phonon scattering. While this approach could be successfully applied to the x = 0.075 sample, the calculated L values for the x = 0.15 sample led to unphysical negative values at high temperatures. This inadequacy of the present model to calculate L is due to the multiband nature of the valence band structure of this compound that results in lower L values than those predicted for a highly-degenerate hole gas using the SPB model. This difficulty in determining the lattice contribution has been highlighted in several thermoelectric materials, such as SnTe, for which the presence of several electronic bands tends to lower the L values despite the strongly degenerate nature of the compound.[60–63]

The temperature dependence of κ_L for the x = 0.075 sample is shown in **Figure 10d**. For comparison purposes, the data of the pristine compound has been added. For both compounds, the strong decrease with increasing temperature reflects the dominance of phonon-phonon Umklapp scattering processes, which leads to $\kappa_L(T)$ curves nearly following a T^{-1} law. The lower κ_L values observed in the x = 0.075 sample compared to those of Cu_2SnS_3 suggests a more pronounced disordered character of the former, in agreement by the Hall mobility data. This increased disorder leads to a strong enhancement of point-defect scattering, yielding a minimum κ_L value of 0.55 W m^{-1} K^{-1} at 700 K. These remarkably very low values are similar to those typically observed in tetrahedrites and in strongly-disordered colusites.[52,64–67]

The temperature dependence of the dimensionless thermoelectric figure of merit, *ZT*, of the $Cu_{2+x}Sn_{1-x}S_3$ compounds is shown in **Figure 10f**. The *ZT* values increase monotonically for all the

compositions with increasing temperature. The $Cu_{2.075}Sn_{0.925}S_3$ sample exhibits the highest peak *ZT* value of 0.3 at 700 K, that originates from the favorable combination of high power factor and very low lattice thermal conductivity. This maximum *ZT* remains nevertheless moderate, compared to those achieved in optimized tetrahedrites and colusites,[21,64,65,68] due to the high metallic character of this compound.

4. CONCLUSIONS

We have discovered an ordered sphalerite derivative $Cu_5Sn_2S_7$ ($C2$ monoclinic), in the Cu-Sn-S diagram and clarified the complex crystal chemistry in this class of materials. The phase obtained for x = 0.15 corresponds to $Cu_5Sn_2S_7$ and is stabilized by an interplay between structure and stoichiometry that governs the ordering of Cu and Sn on the cationic sublattice. The $C2$ phase includes an interacting pair of Sn centered tetrahedra, which favors the delocalization of the holes of the surrounding sulfur atoms (**Figure 12**). The electrostatic interaction between the tetrahedra dimers, due to the excess of positive charges on Sn, energetically favors a long-range ordering. The combination of (1) long range order, (2) a well-connected conductive sphalerite framework enriched by delocalized electrons provided by Sn, and (3) low average effective masses, lead to the largest hole mobility observed so far in *p*-type bulk Cu-Sn-S compounds. This is remarkable when considering the high carrier concentration of 5.75×10^{21} cm^{-3} in $Cu_5Sn_2S_7$. The specific tridimensional $[Cu_5S_7]_\infty$ tetrahedral framework forming tunnels running along the *c*-axis, where the Sn_2S_7 dimers are located, favors a high carrier mobility in the conductive network. The plot of the mobility versus carrier concentration ($p > 1\times10^{21}$ cm^{-3}) at 300 K (**Figure 13)** highlights the special character of this phase among related *p*-type bulk Cu-based ternary and quaternary sulfides. Adjustment of the hole concentration through aliovalent substitutions should also lead to significant

optimization of the *ZT*, possibly making this ternary compound competitive among the highly-efficient, sulfur-based thermoelectric materials developed so far. In this regard, electronic band structure calculations have indicated that substitutions on the Sn site might be beneficial for optimizing the hole concentration and preserving the multivalence band structure that tends to favor high Seebeck coefficients, while maintaining a high hole mobility in the "Cu-S" conductive network. Such cationic substitution can then provide an additional tuning knob to increase the number of electrons, moving the Fermi level upward, and partially filling up the two holes per unit cell (Z = 2). Interestingly, the complete filling of the valence bands would lead to a semiconductor with a bandgap of around 1 eV, which is in an optimal range for photovoltaic application. The hole mobility should be also increased due to the decrease in the carrier concentration, which is of interest for optimizing the PV performances.

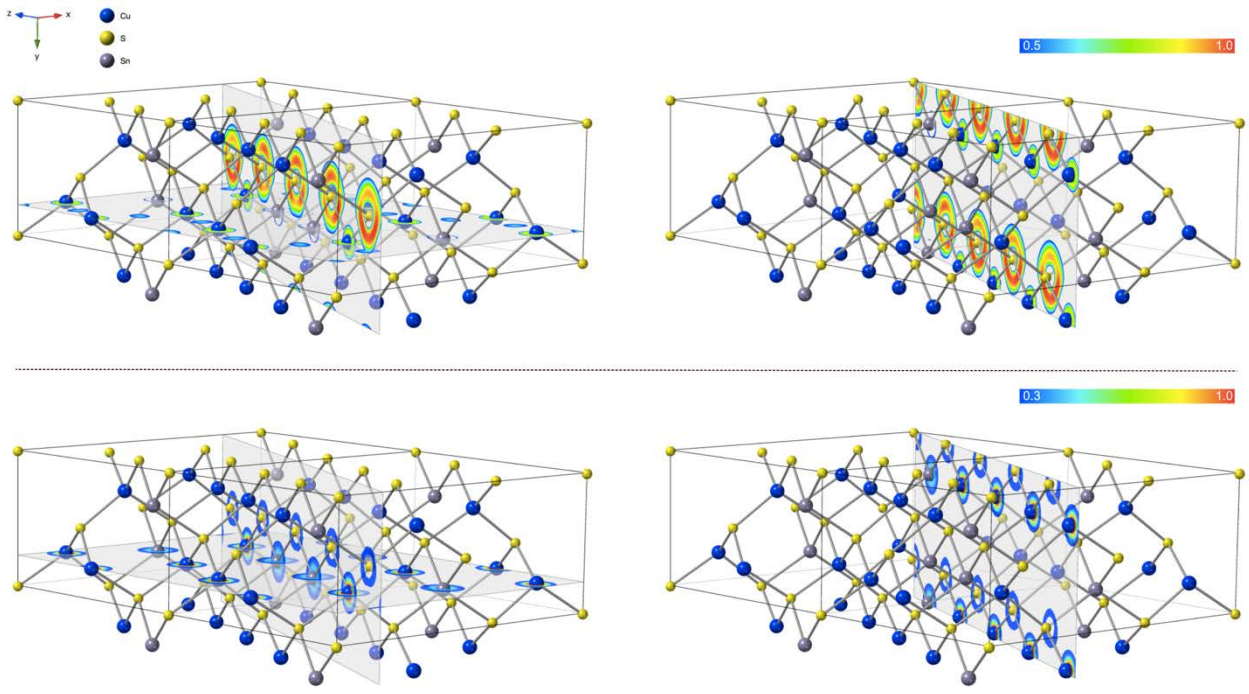

Figure 12. Contour of the Electron Localization Factor (ELF) (top) and charge density (bottom) for selected planes of monoclinic $C2$ $Cu_5Sn_2S_7$. Values for the ELF range between 0 and 1: ELF = 0.5 (blue contours) indicates free electron behavior and ELF = 1.0 (red contour) indicates perfect

localization. Values smaller than 0.5 are less significant and usually point to small local electron density. Values for the charge density range between 0.3 (blue) and 1.0 (red).

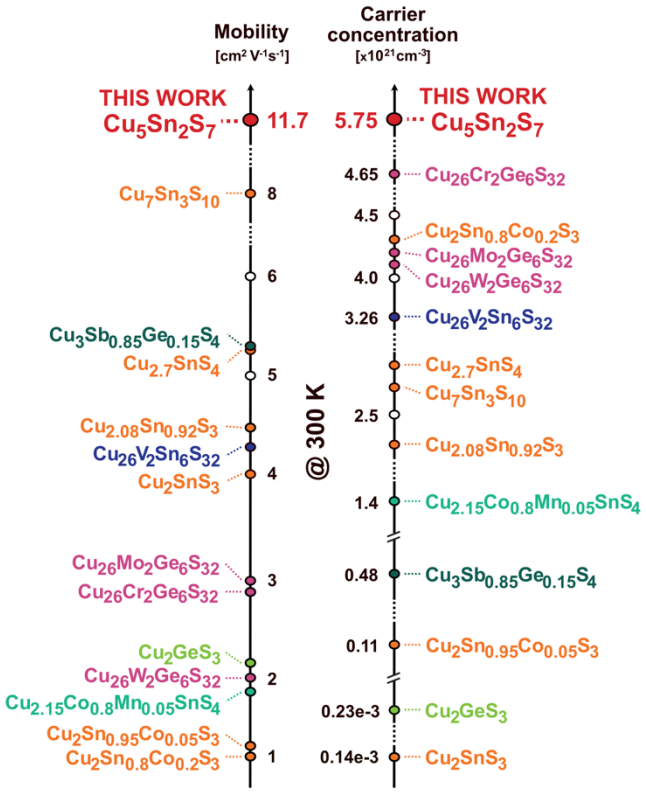

Figure 13. Current state-of-the-art mobility (left) and carrier concentration (right) values at 300 K in *p*-type bulk copper-based sulfides. Different families are highlighted with different colors. Among them we underline colusites (violet and blue) and Cu_2SnS_3 derivatives (orange), present work in red.[1,3,17,20,21,66,69–73]

Acknowledgments

The authors gratefully thank Christelle Bilot and Jerôme Lecourt for technical support. The authors acknowledge SOLEIL for provision of synchrotron radiation facilities and would like to thank Andrea Zitolo and Gautier Landrot for assistance in using beamline SAMBA. The authors

acknowledge the financial support of the French Agence Nationale de la Recherche LabEx EMC3 through the Project FACTO (Grant No. ANR-10-LABX-09-01), the Normandy Region (Réseau d'Intérêt Normand - Label d'excellence), CARNOT ESP and FEDER.

Conflict of Interest

The authors declare no conflict of interest.

Authors contribution

V. P. K : conceptualization, investigation, validation,visualization, writing – review & editing
P.L. : conceptualization, investigation, validation, visualization, writing – original draft, writing – review & editing
V. C. : formal analysis, investigation, visualization, writing – review & editing
G. G. : investigation, visualization, writing – review & editing
O. I. L. : investigation, validation, visualization, writing – review & editing
P. B. : investigation, validation, visualization, writing – review & editing
B. R. : conceptualization, writing – original draft, writing – review & editing
R. A. R. A. O. : formal analysis, writing – review & editing
M. F. : conceptualization, formal analysis, visualization, writing – review & editing
C. P. : investigation, validation, visualization, writing – review & editing
D. M. : investigation, validation, writing – review & editing
C. C. : investigation, validation, writing – review & editing
B. M. : investigation, validation, visualization, writing – review & editing
J. J. : investigation, funding acquisition, writing – review & editing
E. G : conceptualization, project administration, investigation, validation, funding acquisition, writing – original draft

Keywords: semiconductor • sulphide • mobility • thermoelectric • photovoltaic

REFERENCES

1 Y. Shen, C. Li, R. Huang, R. Tian, Y. Ye, L. Pan, K. Koumoto, R. Zhang, C. Wan and Y. Wang, *Sci. Rep.*, 2016, **6**, 32501.

2 A. C. Lokhande, P. T. Babar, V. C. Karade, M. G. Gang, V. C. Lokhande, C. D. Lokhande and J. H. Kim, *J. Mater. Chem. A*, 2019, **7**, 17118–17182.

3 T. Deng, T. Xing, M. K. Brod, Y. Sheng, P. Qiu, I. Veremchuk, Q. Song, T.-R. Wei, J. Yang, G. J. Snyder, Y. Grin, L. Chen and X. Shi, *Energy Environ. Sci.*, 2020, **13**, 3041–3053.

4 G. H. Moh, *Neues Jahrb. Miner. Abhandl.*, 1976, **128**, 115–188.

5 G. H. Moh, *Carnegie Inst. Washingt.*, 1963, **62**, 197.

6 X. Chen, H. Wada, A. Sato and M. Mieno, *J. Solid State Chem.*, 1998, **139**, 144–151.

7 E. Parthé, *Crystal chemistry of tetrahedral structures*, New York, 1964.

8 J. Rivet, J. Flahaut and P. Laruelle, *Comptes rendus heddomadaires des séances l'Académie des Sci.*, 1963, **257**, 161.

9 S. Jaulmes, J. Rivet and P. Laruelle, *Acta Crystallogr. B*, 1977, **33**, 540–542.

10 G. Kullerud, *Freib. Forschungshefte C*, 1965, **186**, 145–160.

11 R. J. G. Sobbot and G. H. Teh, *Neues Jahrb. Miner. Abhandl.*, 1977, **131**, 23.

12 N. Wang, *Neues Jahrb. Miner. Mh.*, 1974, **9**, 424.

13 N. Wang, *Neues Jahrb. Miner. Mh.*, 1976, **6**, 241.

14 N. Wang, *Neues Jahrb. Miner. Mh.*, 1981, **8**, 337.

15 D. Wu, C. R. Knowles and L. L. Y. Chang, *Mineral. Mag.*, 1986, **50**, 323–325.

16 S. Fiechter, M. Martinez, G. Schmidt, W. Henrion and Y. Tomm, *J. Phys. Chem. Solids*, 2003, **64**, 1859–1862.

17 H. Zhao, X. Xu, C. Li, R. Tian, R. Zhang, R. Huang, Y. Lyu, D. Li, X. Hu, L. Pan and Y.

Wang, *J. Mater. Chem. A*, 2017, **5**, 23267–23275.

18 M. Onoda, X. Chen, A. Sato and H. Wada, *Mater. Res. Bull.*, 2000, **35**, 1563–1570.

19 K. Lohani, H. Nautiyal, N. Ataollahi, C. Fanciulli, I. Sergueev, M. Etter and P. Scardi, *J. Phys. Chem. C*, 2021, **125**, 178–188.

20 T. Deng, P. Qiu, Q. Song, H. Chen, T. Wei, L. Chen, L. Xi, X. Shi and L. Chen, *J. Appl. Phys.*, 2019, **126**, 085111.

21 V. Pavan Kumar, A. R. Supka, P. Lemoine, O. I. Lebedev, B. Raveau, K. Suekuni, V. Nassif, R. Al Rahal Al Orabi, M. Fornari and E. Guilmeau, *Adv. Energy Mater.*, 2019, **9**, 1803249.

22 V. Pavan Kumar, G. Guélou, P. Lemoine, B. Raveau, A. R. Supka, R. Al Rahal Al Orabi, M. Fornari, K. Suekuni and E. Guilmeau, *Angew. Chemie - Int. Ed.*, 2019, **58**, 15455–15463.

23 G. Guélou, P. Lemoine, B. Raveau and E. Guilmeau, *J. Mater. Chem. C*, 2021, **9**, 773–795.

24 W. Schäfer, K. Scheunemann and R. Nitsche, *Mater. Res. Bull.*, 1980, **15**, 933–937.

25 J. Fan, W. Carrillo-cabrera, I. Antonyshyn, Y. Prots, I. Veremchuk, W. Schnelle, C. Drathen, L. Chen and Y. Grin, 2014, **26**, 5244–5251.

26 B. Raveau, *J. Supercond. Nov. Magn.*, 2020, **33**, 259–263.

27 L. Xi, Y. B. Zhang, X. Y. Shi, J. Yang, X. Shi, L. D. Chen, W. Zhang, J. H. Yang and D. J. Singh, *Phys. Rev. B*, 2012, **86**, 155201.

28 B. Sitaud, P. L. Solari, S. Schlutig, I. Llorens and H. Hermange, *J. Nucl. Mater.*, 2012, **425**, 238–243.

29 J. Rodríguez-Carvajal, *Phys. B Condens. Matter*, 1993, **192**, 55–69.

30 T. Roisnel and J. Rodríguez-Carvajal, *Mater. Sci. Forum*, 2001, **378**–**381**, 118–123.

31 E. Mugnaioli, T. Gorelik and U. Kolb, *Ultramicroscopy*, 2009, **109**, 758–765.

32 P. Boullay, L. Palatinus and N. Barrier, *Inorg. Chem.*, 2013, **52**, 6127–6135.

33 L. Palatinus, P. Brázda, M. Jelínek, J. Hrdá, G. Steciuk and M. Klementová, *Acta Crystallogr. Sect. B*, 2019, **75**, 512–522.

34 V. Petříček, M. Dušek and L. Palatinus, *Zeitschrift fur Krist.*, 2014, **229**, 345.

35 V. Briois, E. Fonda, S. Belin, L. Barthe, C. La Fontaine, F. Langlois, M. Ribbens and F. Villain, *SAMBA: The 4–40 keV X-ray absorption spectroscopy beamline at SOLEIL*. *In UVX 2010 - 10e Colloque sur les Sources Cohérentes et Incohérentes UV*, 2011.

36 R. F. Pettifer, M. Borowski and P. W. Loeffen, *J. Synchrotron Radiat.*, 1999, **6**, 217–219.

37 B. Ravel and M. Newville, *J. Synchrotron Radiat.*, 2005, **12**, 537–541.

38 A. L. Ankudinov, B. Ravel, J. J. Rehr and S. D. Conradson, *Phys. Rev. B*, 1998, **58**, 7565–7576.

39 E. Alleno, D. Bérardan, C. Byl, C. Candolfi, R. Daou, R. Decourt, E. Guilmeau, S. Hébert, J. Hejtmanek, B. Lenoir, P. Masschelein, V. Ohorodnichuk, M. Pollet, S. Populoh, D. Ravot, O. Rouleau and M. Soulier, *Rev. Sci. Instrum.*, 2015, **86**, 011301.

40 P. Giannozzi, S. Baroni, N. Bonini, M. Calandra, R. Car, C. Cavazzoni, D. Ceresoli, G. L. Chiarotti, M. Cococcioni, I. Dabo, A. Dal Corso and S. de Gironcoli, *J. Phys. Condens. Matter*, 2009, **21**, 395502.

41 A. R. Supka, T. E. Lyons, L. Liyanage, P. D'Amico, R. Al Rahal Al Orabi, S. Mahatara, P. Gopal, C. Toher, D. Ceresoli, A. Calzolari, S. Curtarolo, M. B. Nardelli and M. Fornari, *Comput. Mater. Sci.*, 2017, **136**, 76–84.

42 D. R. Hamann, *Phys. Rev. B*, 2013, **88**, 85117.

43 L. A. Agapito, S. Curtarolo and M. B. Nardelli, *Phys. Rev. X*, 2015, **5**, 011006.

44 M. Buongiorno Nardelli, F. T. Cerasoli, M. Costa, S. Curtarolo, R. De Gennaro, M.

Fornari, L. Liyanage, A. R. Supka and H. Wang, *Comput. Mater. Sci.*, 2018, **143**, 462–472.

45 C. Lee and X. Gonze, *Phys. Rev. B*, 1995, **51**, 8610–8613.

46 L. Palatinus and A. van der Lee, *J. Appl. Crystallogr.*, 2008, **41**, 975–984.

47 L. Palatinus and G. Chapuis, *J. Appl. Crystallogr.*, 2007, **40**, 786–790.

48 L. Palatinus, C. A. Corrêa, G. Steciuk, D. Jacob, P. Roussel, P. Boullay, M. Klementová, M. Gemmi, J. Kopeček, M. C. Domeneghetti, F. Cámara and V. Petříček, *Acta Crystallogr. Sect. B*, 2015, **71**, 740–751.

49 P. E. Lippens, *Phys. Rev. B*, 1999, **60**, 4576–4586.

50 T. Yamanaka and A. Kato, *Am. Mineral.*, 1976, **61**, 260–265.

51 V. Pavan Kumar, T. Barbier, V. Caignaert, B. Raveau, R. Daou, B. Malaman, G. Le Caër, P. Lemoine and E. Guilmeau, *J. Phys. Chem. C*, 2017, **121**, 16454–16461.

52 C. Candolfi, G. Guélou, C. Bourgès, A. R. Supka, R. Al Rahal Al Orabi, M. Fornari, B. Malaman, G. Le Caër, P. Lemoine, V. Hardy, J. Zanotti, R. Chetty, M. Ohta, K. Suekuni and E. Guilmeau, *Phys. Rev. Mater.*, 2020, **4**, 025404.

53 M. Hegedüs, M. Achimovičová, H. Hui, G. Guélou, P. Lemoine, I. Fourati, J. Juraszek, B. Malaman, P. Baláž and E. Guilmeau, *Dalt. Trans.*, 2020, **49**, 15828–15836.

54 P. E. Lippens, J. Olivier-Fourcade and J. C. Jumas, *Hyperfine Interact.*, 2000, **126**, 137–141.

55 J. L. Wardell, in *Encyclopedia of Inorganic Chemistry*, American Cancer Society, 2006.

56 P. Kumar, R. Nagarajan and R. Sarangi, *J. Mater. Chem. C*, 2013, **1**, 2448–2454.

57 I. D. Brown and K. R. Poeppelmeier, *Structure and Bonding. Bond valences (vol. 158)*, 2014.

58 D. Ibrahim, C. Candolfi, S. Migot, J. Ghanbaja, A. Dauscher, G. Le Caër, B. Malaman, C.

Semprimoschnig and B. Lenoir, *Phys. Rev. Mater.*, 2019, **3**, 85404.

59 H. Xie, H. Wang, C. Fu, Y. Liu, G. J. Snyder, X. Zhao and T. Zhu, *Sci. Rep.*, 2014, **4**, 6888.

60 R. W. McKinney, P. Gorai, V. Stevanović and E. S. Toberer, *J. Mater. Chem. A*, 2017, **5**, 17302–17311.

61 M. Thesberg, H. Kosina and N. Neophytou, *Phys. Rev. B*, 2017, **95**, 125206.

62 L. V. Prokof'eva, A. A. Shabaldin, V. A. Korchagin, S. A. Nemov and Y. I. Ravich, *Semiconductors*, 2008, **42**, 1161.

63 S. Misra, B. Wiendlocha, J. Tobola, F. Fesquet, A. Dauscher, B. Lenoir and C. Candolfi, *J. Mater. Chem. C*, 2020, **8**, 977–988.

64 X. Lu, D. T. Morelli, Y. Xia, F. Zhou, V. Ozolins, H. Chi, X. Zhou and C. Uher, *Adv. Energy Mater.*, 2013, **3**, 342–348.

65 K. Suekuni, K. Tsuruta, M. Kunii, H. Nishiate, E. Nishibori, S. Maki, M. Ohta, A. Yamamoto and M. Koyano, *J. Appl. Phys.*, 2013, **113**, 043712.

66 C. Bourgès, Y. Bouyrie, A. R. Supka, R. Al Rahal Al Orabi, P. Lemoine, O. I. Lebedev, M. Ohta, K. Suekuni, V. Nassif, V. Hardy, R. Daou, Y. Miyazaki, M. Fornari and E. Guilmeau, *J. Am. Chem. Soc.*, 2018, **140**, 2186–2195.

67 K. Suekuni, Y. Shimizu, E. Nishibori, H. Kasai, H. Saito, D. Yoshimoto, K. Hashikuni, Y. Bouyrie, R. Chetty, M. Ohta, E. Guilmeau, T. Takabatake, K. Watanabe and M. Ohtaki, *J. Mater. Chem. A*, 2019, **7**, 228–235.

68 K. Suekuni, F. S. Kim, H. Nishiate, M. Ohta, H. I. Tanaka and T. Takabatake, *Appl. Phys. Lett.*, 2014, **105**, 132107.

69 Y. Goto, Y. Sakai, Y. Kamihara and M. Matoba, *J. Phys. Soc. Japan*, 2015, **84**, 44706.

70 Y. Goto, Y. Sakai, Y. Kamihara and M. Matoba, *Jpn. J. Appl. Phys.*, 2015, **54**, 21801.

71 D. Zhang, J. Yang, Q. Jiang, Z. Zhou, X. Li, J. Xin, A. Basit, Y. Ren and X. He, *Nano Energy*, 2017, **36**, 156–165.

72 K. Chen, B. Du, N. Bonini, C. Weber, H. Yan and M. J. Reece, *J. Phys. Chem. C*, 2016, **120**, 27135–27140.

73 S. Jacob, B. Delatouche, D. Péré, A. Jacob and R. Chmielowski, *Mater. Today Proc.*, 2017, **4**, 12349–12359.